Chapter 9
On the Kinematics of Sheet and Cloud Cavitation and Related Erosion

Peter F. Pelz, Thomas Keil and Gerhard Ludwig

Abstract The influence of flow parameters such as cavitation number and Reynolds number on the cavitating cloud behavior and aggressiveness is analysed in an experimental work. The focused geometry is a convergent-divergent nozzle with a given radius of curvature at the minimum cross section. By means of a high-speed camera the kinematics of cloud cavitation is visualized. The shape of the cloud is a horse shoe (U-shaped) with two legs ending at the material surface which is in agreement with the Helmholtz vortex theorem. Indeed it is worthwhile to look at the cavitation cloud as a ring vortex whose second half is a mirror vortex within the material. Due to the convection flow, the legs of the vortex are elongated and hence the rotational speed of the vortex core will increase. Thus cavitation bubbles will concentrate within the legs of the vortex and that behavior is observed in the cavitation experiments. The aggressiveness of the cloud is quantified by using soft metal inserts adapted on the nozzle geometry. The interpretation of the plastic deformation, called pits, is done with a 2-dimensional optical measurement system, which is developed to scan large and curved surfaces. In this way damage maps are obtained. Consequently dimensional analysis is used to analyse and generalize the experimental results. Thus a critical Reynolds number is found for the transition from sheet to cloud cavitation. Further an upper limit for the Strouhal number exists for the given geometry. A physical model for the critical Reynolds number is given elsewhere [1]. Also a model for the dynamics of the observed stretched cloud with circulation is published by Buttenbender and Pelz [2].

P. F. Pelz (✉) · T. Keil · G. Ludwig
Technische Universität, Darmstadt, Germany
e-mail: peter.pelz@fst.tu-darmstadt.de

K.-H. Kim et al. (eds.), *Advanced Experimental and Numerical Techniques for Cavitation Erosion Prediction*, Fluid Mechanics and Its Applications 106,
DOI: 10.1007/978-94-017-8539-6_9,

9.1 Introduction

One of the more aggressive cavitation forms is cloud cavitation which is observed above a critical Reynolds number as will be shown in this paper. The high aggressiveness of cloud cavitation was reported by several researchers (e.g. [3–6]). It is now understood that the cloud plays a key role in the temporal and spatial energy focusing cascade which is essential for the cavitation erosion process. The stationary energy flux of the incoming flow is concentrated in time and space in the form of clouds. The state of the collapse and the time delay depends on the growth rate, the initial size and the initial bubble population of the cloud [2]. When the cloud collapses the second energy focusing process starts: Like a single bubble when collapsing the cloud imposes a sink flow and focuses the kinetic energy of the surrounding fluid in its center.

The intensity of the collapse and thus the aggressiveness is determined by the dynamic behavior and by the type of the structures occurring. Kawanami et al. [7] employed a model to describe the shape of a cloud by a U-shaped vortex. Their investigations base on holographic experiments in a cavitation tunnel. Similar observations were done by Joussellin et al. [8]. The circulation of the cloud can be observed by high-speed visualization (Kawanami et al. [9]).

The aggressiveness of cavitation erosion is assessed by using soft metal layers, as material sensors. This approach enables the evaluation of damage distributions and damage intensities. To quantify the effective damage energy, a pit-count measurement system is used, which detects the size and the position of each pit on the damaged surface. The effective damage energy and thereby the cavitation aggressiveness is quantified by a dimensionless damage function.

9.2 Experimental Set Up and Dimensionless Products

The needs for the test rig are (i) an excellent optical accessibility, (ii) the possibility to vary the geometry curvature and (iii) to provide an installation-opportunity for soft metal layers which serve as material sensors.

The optical access (i) is realized by a channel having rectangular cross section and walls completely made of acrylic glass. The high-speed observations are illuminated with a stroboscope for the top view perspective. For the side view perspective a laser light sheet is used. The copper layer (iii) is placed directly downstream of the narrowest cross-sectional area. The analyzed area is close to the cloud collapse location downstream of the sheet cavity.

To initiate evenly the cavitation over the whole nozzle width, an obstacle with rectangular cross section seen in Fig. 9.1 is placed in the smallest cross section area. First experiments show that the side wall friction influence due to surface roughness is small in comparison to the obstacle influence and is not visible in the experiments. Flows without this obstacle would generate single bubbles over the

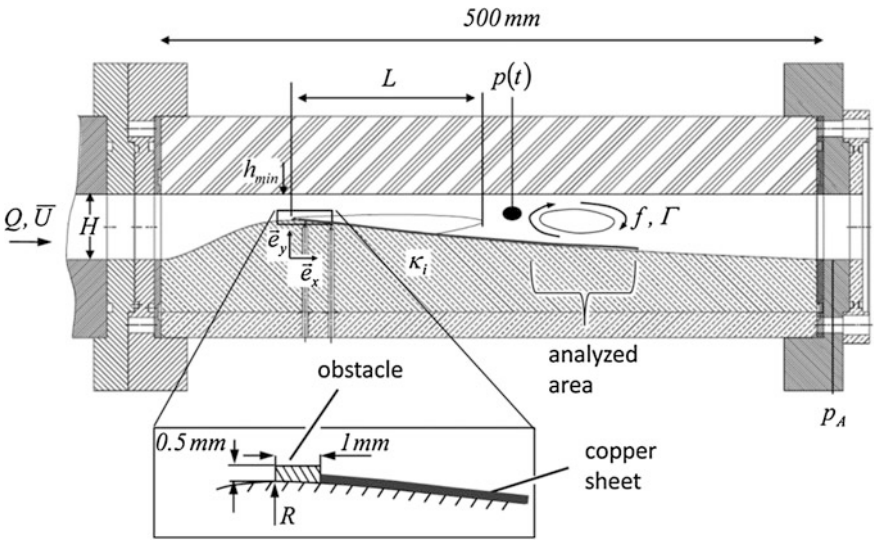

Fig. 9.1 Nozzle test rig at the Chair of Fluid Systems Technology

nozzle width and two cavitation zones in the corners between contour and vertical side walls of the tunnel instead a close cavity zone as shown in Fig. 9.2.

The nozzle shape is given by the following function where the height h and the axial length x are made dimensionless by the channel height $H = 50$ mm:

$$h^+(x^+) = \frac{const.}{\exp\left(\frac{x^+}{\kappa_1}\right) + \exp\left(-\frac{x^+}{\kappa_2}\right)}, \tag{9.1}$$

where superscript + indicates a non-dimensional quantity.

The non-dimension radius of curvature in the smallest cross section area is determined by the two free parameters κ_1 and κ_2. The influence of both parameters

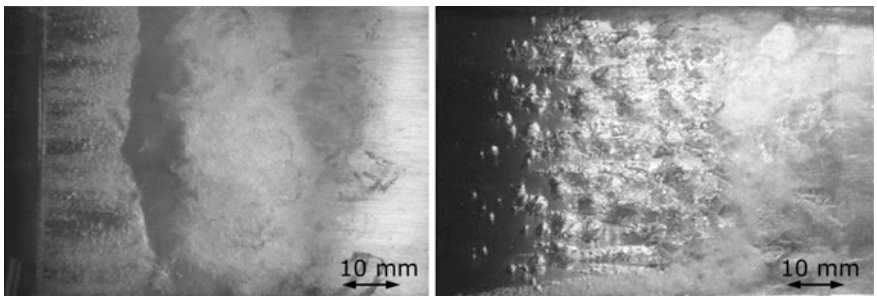

Fig. 9.2 Influence of the obstacle in the smallest cross section area for $R^+ = 2.5$, $Re = 3.1 \times 10^5$ and $\sigma = 6.05$. *Left* with obstacle, *right* without obstacle

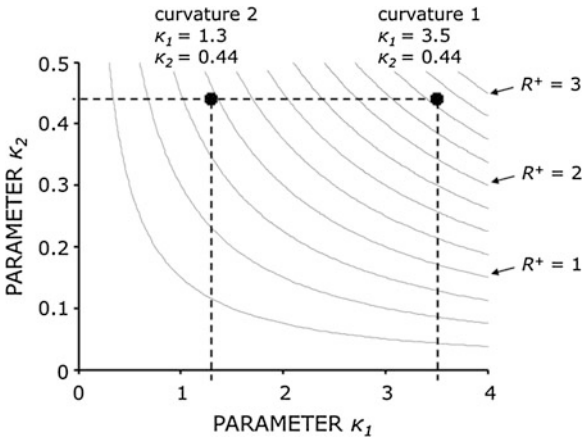

Fig. 9.3 Radius of curvature for the shape function, Eq. (9.1), and parameters of curvature 1 and 2

on the radius of curvature at the smallest cross section ($x = 0$) is shown in Fig. 9.3. The filled circles indicate the two geometries being under research. Within this contribution two cavitating flows with a radius of curvature of $R^+ = 2.5$ and $R^+ = 0.95$ are presented and discussed. The damage analysis was only done for the radius of curvature $R^+ = 2.5$.

The cavitation behavior is influenced by the Reynolds number and the cavitation number, based on the outlet pressure p_A and the cross section averaged flow velocity $\overline{U}$, which is varied between 3.9 and 7 m/s (Fig. 9.1):

$$\sigma = \frac{p_A - p_V}{\frac{1}{2}\rho\,\overline{U}^2}, \tag{9.2}$$

$$Re = \frac{\overline{U}H}{\nu}, \tag{9.3}$$

where ν denotes the kinematic viscosity, ρ the density and p_V the vapor pressure of water. The channel outlet is used as the reference location because only the pressure downstream of the cavitation zone influences the cavity in the case of constant flow rate and presence of cavitation. The local pressure in the smallest cross section is approximately the vapor pressure while the pressure difference is the same for constant velocity in the convergent part.

A single pressure sensor with an eigenfrequency of 125 kHz is flush-mounted in a fixed position in the side wall of the channel 65 mm downstream of the smallest cross section. The sensor records pressure fluctuation caused by the cloud collapses and helps to detect typical frequencies of the flow.

For cloud cavitation the most relevant physical parameters are the shedding frequency f of the cavitation cloud, the typical size L of the sheet and the circulation Γ of the cloud which is discussed in the next section. The measured associated dimensionless relations are:

$$\frac{f H}{\overline{U}} = St(Re,\ \sigma,\ \kappa_i), \tag{9.4}$$

$$\frac{L}{H} = \lambda(Re,\ \sigma,\ \kappa_i), \tag{9.5}$$

$$\frac{\Gamma}{\overline{U} H} = \gamma(Re,\ \sigma,\ \kappa_i). \tag{9.6}$$

With Eqs. (9.4–9.6) the largest scales of the periodic cavitation process are given.

9.3 Experimental Results

9.3.1 Observations

The high-speed images from the top view of the channel (Fig. 9.4) show the sheet and the cloud cavitation for a radius of curvature $R^+ = 2.5$. The operating conditions given by $\sigma = 5.7$ and $Re = 3.13 \times 10^5$ are such that cloud cavitation is dominant. This corresponds to a flow velocity of $\overline{U} = 6.3$ m/s in the outlet section area. The process is evaluated by a software tool detecting the front edge of the sheet and of the cloud.

The cycle starts by the growth of the cavitation sheet to its maximum sheet length L (Fig. 9.4a–e). The cavity starts growing with its origin fixed at the inserted wire along the rectangular cross section. While the sheet cavity reaches its maximum length, the re-entrant jet flows from a stagnation line on the surface. The front of the re-entrant jet is clearly visible in Fig. 9.4e–f. In the case of periodic cloud cavitation ($Re > Re_{crit}$) there is enough time for the upstream spread of the re-entrant jet to reach the leading edge of the sheet (Fig. 9.4a next period).

During the growth process, the cloud is observed in Fig. 9.4a–c. The white dotted line indicates the most downstream edge of the cloud. The cloud remains in the wake of the growing sheet cavitation, which can be seen by the stagnation of the rolled-up cloud. During this period, the cloud is imposed a circulation and forms a vortex with contact to the side walls. When this happen a cloud separates and the sheet starts again with the growth as described above.

Due to the Helmholtz vortex theorem the vortex has either to be closed at infinity or being a ring at every moment. This is the physical reason for the often seen U-shaped cloud (Fig. 9.4c–d).

The lower pressure in the vortex core leads to a decrease of the static pressure, which is measured by the pressure sensor installed at the channel wall downstream of the smallest cross section area. Actual pressure value for each picture is shown in the middle of the cross of the diagram. Past pressure values are demonstrated on the left hand side of the cross.

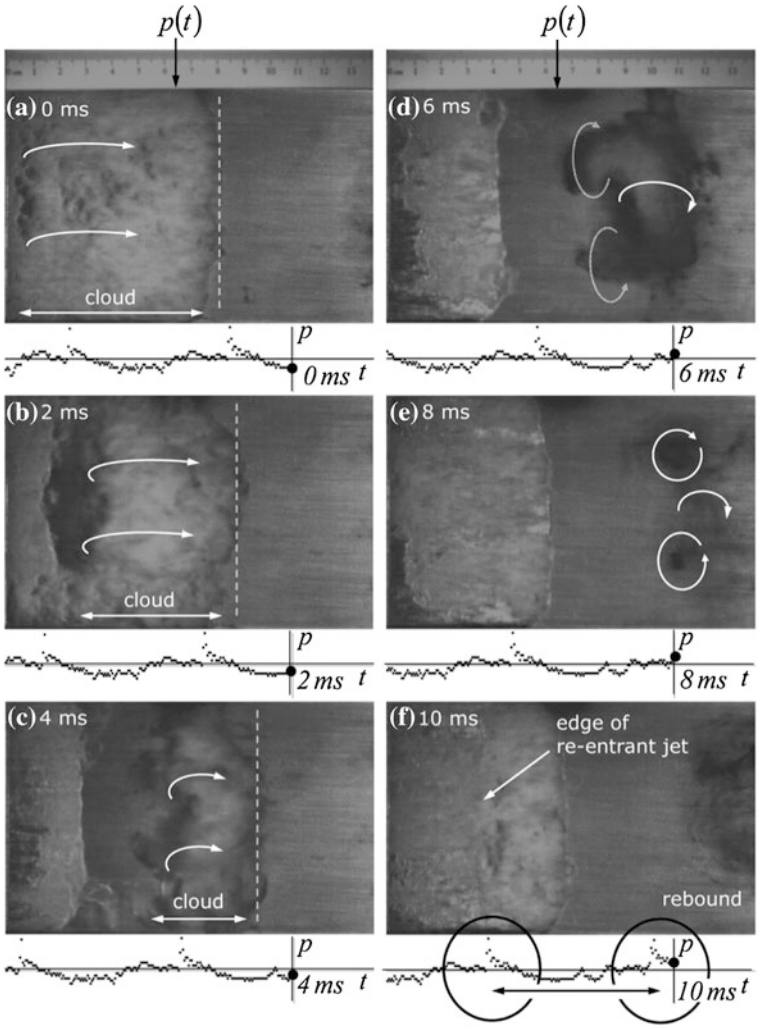

Fig. 9.4 High speed visualization for $Re = 3.13 \times 10^5$, $\sigma = 5.7$ and $R^+ = 2.5$. The actual pressure value is shown in the cross of the diagram *below* the pictures. The past pressure signal corresponds to the *left hand side* of the cross. The shedding frequency is about 49 Hz

The cloud collapse produces a pressure peak, which is also recorded and qualitatively shown in Fig. 9.4f. The collapse of the cloud seen in the pressure peak of Fig. 9.4f is between 8 and 10 ms pictures. The periodic behavior of the flow is visible from the pressure timeline shown in Fig. 9.4 as well.

The Fourier transform of time histories of pressure signal and of position of typical edges (detect by image processing) in high-speed videos are shown in Fig. 9.5 for one typical operating condition in which the characteristic frequency is 60 Hz. The cloud shedding frequency depends on the time delay until the sheet

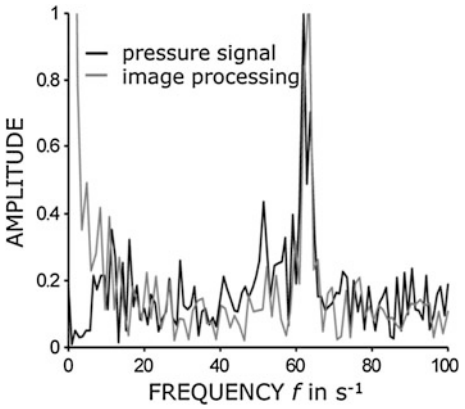

Fig. 9.5 Fourier transform of the pressure history and the position of the sheet cavity front for $R^+ = 2.5$, $Re = 3.13 \times 10^5$ and $\sigma = 5.7$ for the first curvature

reaches its maximum length plus the time delay until the re-entrant jet reaches the leading edge. Both times are determined by the velocity field of the sheet cavity and the sheet cavity length. The analysis of both signals show a clear typical frequency associated with the cloud shedding.

The cavitation behavior changes by a change of the geometry. In the following, the influence of the curvature is discussed on the base of high-speed videos. Compared to the geometry above, the second one has a different parameter κ_1 whereas κ_2 is constant and thus changes the dimensionless radius of curvature in the smallest cross section area (Fig. 9.3). In this case the divergent part of the nozzle is changed dramatically which leads to more detachment flow downstream of the smallest cross section area.

The sheet cavitation could not be detected, which makes the analysis of the cavitation behavior of curvature 2 ($R^+ = 0.95$) more difficult. Instead of a sheet cavity a formation of cavitating vortices close to the obstacle could be seen. The vortices merge together and form a bigger one, which also collapses in the downstream flow. This vortex merging process is marked in Fig. 9.6. Maybe this is the reason that the frequency is irregular so that no typical periodic cloud shedding can be detected. In Fig. 9.7 the Fourier transformation of the pressure signal shows a frequency band from 0 to 100 kHz and its harmonic frequencies.

In the following the influence of Reynolds number and cavitation number on the dimensionless products for the first curvature ($R^+ = 2.5$) are discussed.

9.3.2 *Strouhal Number Versus Reynolds and Cavitation Number*

Figure 9.8 shows the Strouhal number (see Eq. (9.4)) as a function of the cavitation and Reynolds numbers. There are two characteristic flow regimes (shown in Figs. 9.8, 9.9). For a given cavitation number there is a critical Reynolds number.

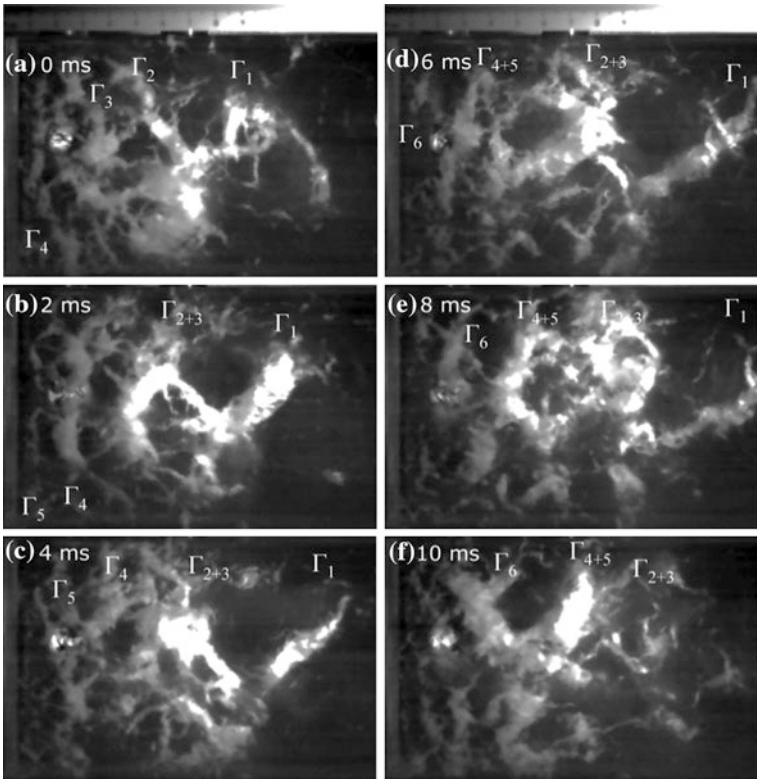

Fig. 9.6 High-speed video of the cavitating flow for a smaller radius of the curvature $R^+ = 0.95$ and for $Re = 3.13 \times 10^5$ and $\sigma = 5.7$

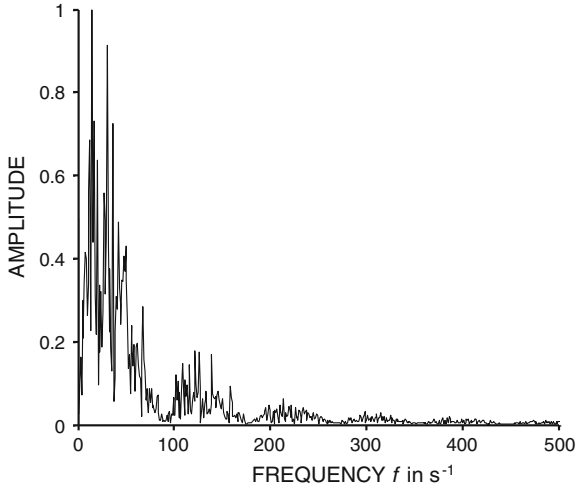

Fig. 9.7 Fourier transform of the pressure history for $Re = 3.13 \times 10^5$ and $\sigma = 5.7$ for $R^+ = 0.95$

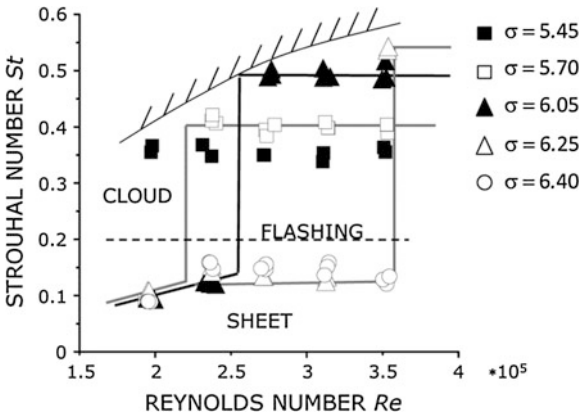

Fig. 9.8 Transition from sheet to cloud cavitation for $R^+ = 2.5$

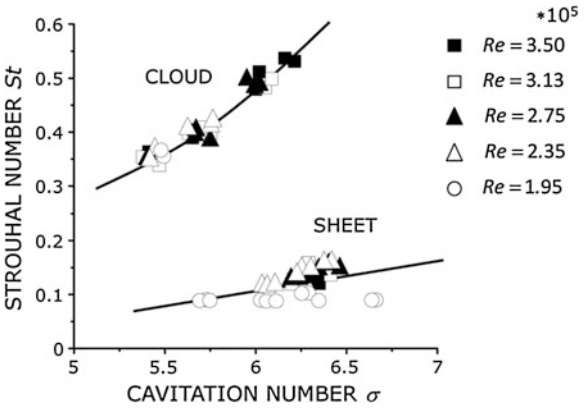

Fig. 9.9 Strouhal number versus cavitation number for $R^+ = 2.5$

(i) Below the critical Reynolds number sheet cavitation without cloud shedding could be observed. (ii) Above that critical Reynolds number cloud cavitation is observed. The Strouhal number is in that case independent of the Reynolds number. Hence there should be no dependence on the size of the device in that flow regime. The research about the critical Reynolds-effect is not finished yet. Further experiments with glycol–water mixture to analyse a viscosity effect are in the planning stage.

A critical velocity was first described by Arndt [10]. In this paper, the velocity is made dimensionless by the kinematic viscosity and the channel height (i.e. Reynolds number).

For the highest cavitation number of 6.4, a critical Reynolds number could not be observed. (But there might be such a number outside the operating range of our test rig.)

By reducing the cavitation number at a given Reynolds number the sheet cavity length increases until the stability limit is reached again. The transition is associated with a sudden increase of the Strouhal number from its minimum to its

maximum value at a given Reynolds number. The limiting curve is roughly indicated in Fig. 9.8 by the upper line. A further reduction of the cavitation number leads to an enlargement of the sheet cavity length and thus to a reduction of the Strouhal number. The decrease of the cavitation number finally leads to full cavitation (flashing) just above the dotted line in Fig. 9.8. In this case the experimental set up is filled with vapor and the outlet pressure corresponds to the pressure in the smallest cross section area.

Figure 9.9 shows the dependence of the Strouhal number on the cavitation number.

9.3.3 Sheet Cavity Length and Circulation of the Cloud

Figure 9.10 shows the maximum sheet cavity length L as a function of the cavitation number. In Fig. 9.11 typical dimensionless velocities are characterized for the cloud cavitation regime as a function of the cavitation number. The markers for different Reynolds numbers form clusters which demonstrate that the cloud cavitation is independent of the Reynolds number as again Figs. 9.8 and 9.9 indicate. These general results justify model tests of pumps or turbines with respect to cloud cavitation.

The growing size of the cavitation sheet for a decrease of the cavitation number causes a throttling of the flow. A simple fluid mechanical model based on Carnot's shock loss [1] is sufficiently accurate to predict the experimental results (solid line in Fig. 9.10).

Figure 9.11 shows the mean velocities of the sheet cavity growth $u_{sheet}/\overline{U}$ and of the re-entrant jet $u_{jet}/\overline{U}$. Both quantities are calculated with the time needed for the sheet cavity to reach its maximum length and the time needed for the re-entrant jet to reach the leading edge. The sheet and jet velocities are determined by means of visualizations and are time averaged velocities. As Fig. 9.11 shows, the velocities do not depend on the Reynolds number. Another point to mention is the difference between the velocities which cannot be explained by classical free-

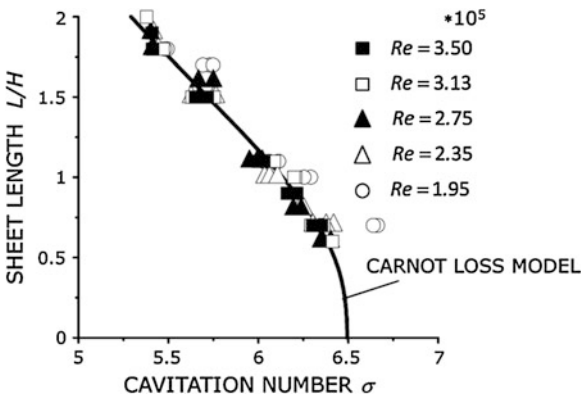

Fig. 9.10 Sheet length versus cavitation number for $R^+ = 2.5$. The Reynolds number has no influence on the sheet length. The *solid line* indicates a Carnot loss model

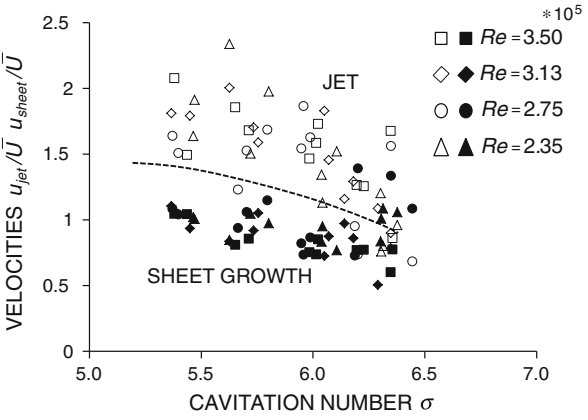

Fig. 9.11 Mean velocity of the growing sheet cavitation and the velocity of the re-entrant jet for $R^+ = 2.5$

streamline theory and depends on other physical effects which are beyond the scope of this work. The mean sheet cavity growth velocity is close to the velocity of the incoming flow. The mean flow velocity at the minimal cross section is by a factor of 2.5 higher than the sheet cavity growth velocity.

To quantify the circulation, the closed integral over the sheet is evaluated by using the mean values of the velocity in the smallest cross section area which is nearly the velocity above the sheet cavity and of the determined velocity of the re-entrant jet u_{jet},

$$\gamma = \frac{\Gamma}{\overline{U}H} = \frac{L}{H}\left(\frac{H}{H_{\min}} + \frac{u_{jet}}{\overline{U}}\right). \tag{9.7}$$

An increased cavitation length, i.e. decreased cavitation number, results in an increased circulation number as shown in Fig. 9.12.

To conclude, as soon as a critical Reynolds number is reached, there is a periodic cloud shedding and the Reynolds number vanishes on the right hand side of Eqs. (9.4–9.6) which then become $f\overline{U}/H = St(\sigma, \kappa_i), L/H = \lambda(\sigma, \kappa_i)$, $\Gamma/\overline{U}H = \gamma(\sigma, \kappa_i)$.

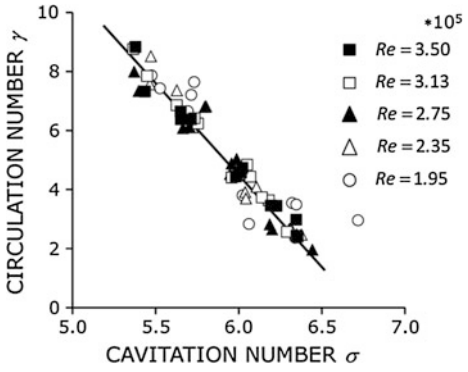

Fig. 9.12 Dimensionless circulation number versus cavitation number for $R^+ = 2.5$

9.4 Plastic Deformation of Solid Surface Due to Cloud Cavitation

9.4.1 Automated Pit-Count System

The pit-count technique used at the Chair of Fluid Systems Technology is able to detect plastic deformations on polished metal surfaces. It is a 2-D optical technique which provides information regarding pit area only (Lohrberg [11]). Curved surfaces are scanned by an all-in-focus algorithm with a completely automated system shown in Fig. 9.13. This allows generating sharp pictures although the surface is deformed and causes different focal points. A microscope moves in three coordinates controlled by three stepper motors. The surface is scanned before and after a cavitation experiment. By comparing the two scans, a filter algorithm is implemented to distinguish between material defects and pits, which are the result of collapsing cavitation bubbles. Such a pit is shown in Fig. 9.14.

The pit-count software gives finally a damage map of the curved surface. The creation of damage maps with a local damage distribution with known radius and position of all plastic deformation are possible. The damage energy can be calculated by using an empirical relationship developed and used by Lohrberg [11],

$$E = \vartheta L_m^3 \sum \left(1 + \frac{r_i}{l_m}\right)^3, \tag{9.8}$$

where ϑ is the yield stress of the material, L_m and l_m are two material typical lengths. The product ϑL_m^3 is the minimum energy to generate a pit, which is equal

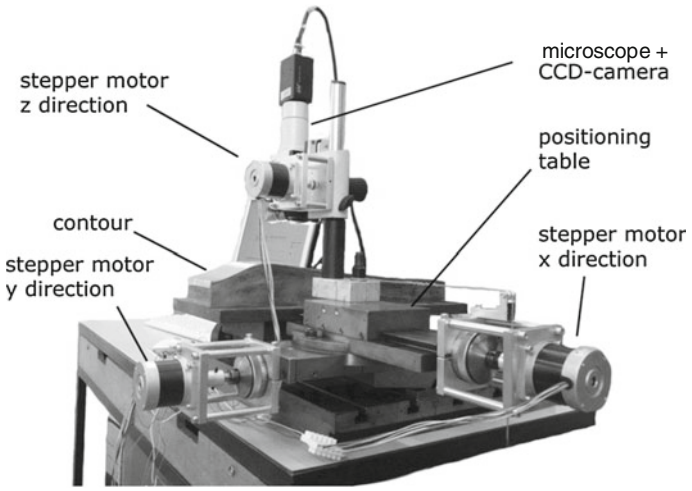

Fig. 9.13 Fully automated pit-count system at the Chair of Fluid Systems Technology

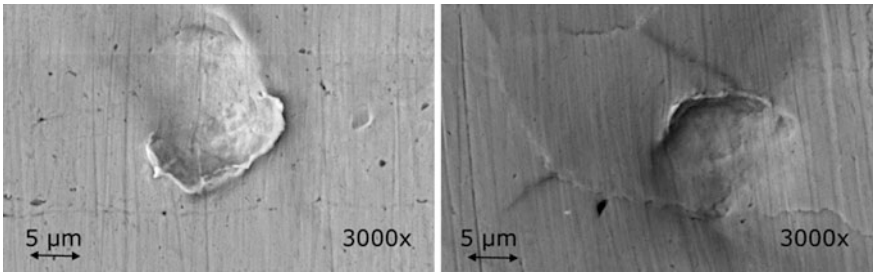

Fig. 9.14 Plastic deformations of a copper surface after 30 min (*left*) and dislocation movements of grains after 300 min (*right*), $\sigma = 0.112$

to the energy to get over the elastic limit. r_i is the pit radius which is made dimensionless with a material dependent constant l_m which gives an empirical relation between the pit radius and the plastic deformed volume. All empirical relations are found out by Lohrberg [11].

9.4.2 Damage Maps

Pit count measurements are carried out for Reynolds numbers 2.75×10^5 and 3.5×10^5, three cavitation numbers 5.45, 5.7, 6.05 and a dimensionless radius $R^+ = 2.5$. Figure 9.15 (left) shows those operation points to lay completely within the cloud regime.

Figure 9.15 (right) shows the damaged surface in percent for a Reynolds number of 2.75×10^5 and the three cavitation numbers. The exposure time T= 90 min is made dimensionless by the shedding frequency. Thus fT gives the number of clouds shed by the sheet cavity during the exposure time. The number of load cycles is given for each experiment in Figs. 9.15 and 9.16.

As expected, a smaller cavitation number results in an increased cavitation zone and thus an increased damage during the exposure time. A smaller sheet cavity with a higher frequency and thus more damage cycles leads to less damage than a large sheet with a lower frequency as can be seen qualitatively in Fig. 9.15.

Figure 9.16 shows the experimental results for the larger Reynolds number of 3.5×10^5. The load cycles are given within the pictures. In all damage pictures a typical erosion of a collapsed U-shaped cavitation vortex can be observed.

To compare the experimental results the deformation energy is accumulated for the whole polished surface using the empirical relation (9.8).

To make different flow conditions comparable, it is useful to normalize the deformation as:

$$\frac{E}{\rho \overline{U}^2 H^3 f T} = \pi(Re,\ \sigma,\ \kappa_i)\,. \tag{9.9}$$

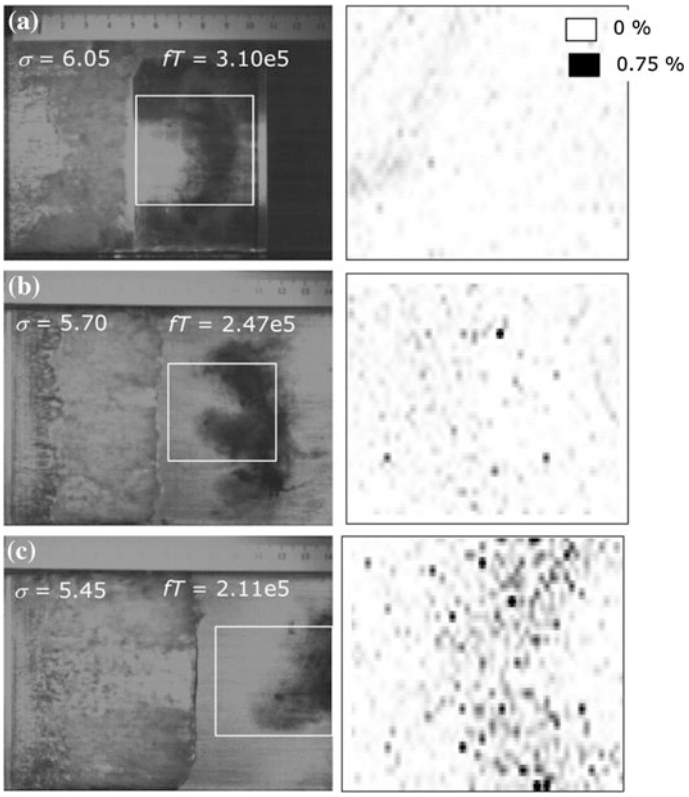

Fig. 9.15 Damage maps for the cavitation numbers 5.45, 5.7, 6.05 at a small Reynolds number of 2.75×10^5 and $R^+ = 2.5$. Each pixel represents the information of several single pictures. The *colour* indicates the damage evaluated by an analysis of the single pictures

In order to compare the aggressiveness of operating points, the non-dimensional energy is based on the number of damage cycles fTin Eq. (9.9). The result is shown in Fig. 9.17 where the accumulated dimensionless damage energy per cycle is given as a function of the cavitation number.

Up to $Re = 3.5 \times 10^5$ at the lowest cavitation number (see damage map shown in Fig. 9.15c), all results are on one line. To show the influence of the Reynolds number for small cavitation numbers an operating point for a Reynolds number at 2.35×10^5 is added in the measurement program.

Figure 9.18 shows the position of center of the damage given in Figs. 9.15 and 9.16 and the maximum sheet cavity length normalized with the channel height. The damage position is primarily influenced by the cavitation number and thus by the sheet cavity length.

The position of the maximum cavity length corresponds to the location of the cloud collapse.

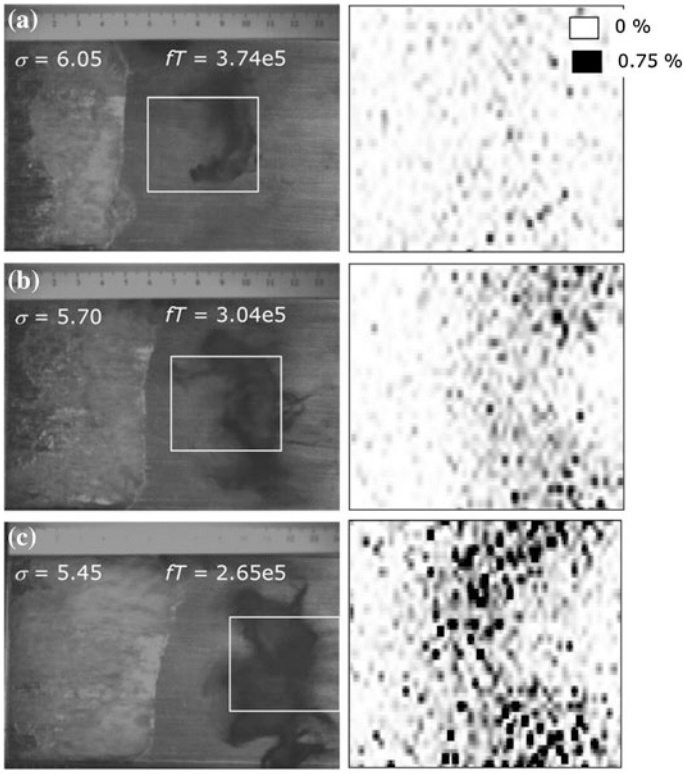

Fig. 9.16 Damage maps for the cavitation numbers 5.45, 5.7, 6.05 at a small Reynolds number of 3.5×10^5 and $R^+ = 2.5$. Each pixel represents the information of several single pictures. The *colour* indicates the damage evaluated by an analysis of the single pictures

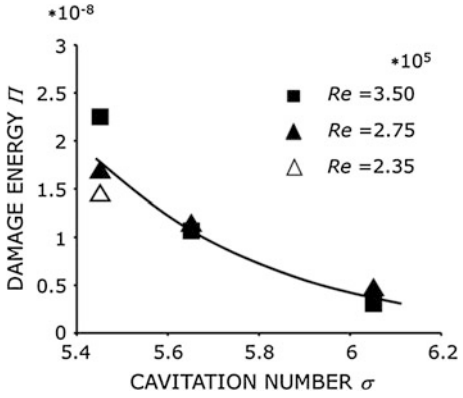

Fig. 9.17 Dimensionless damage energy per damage cycle for $R^+ = 2.5$

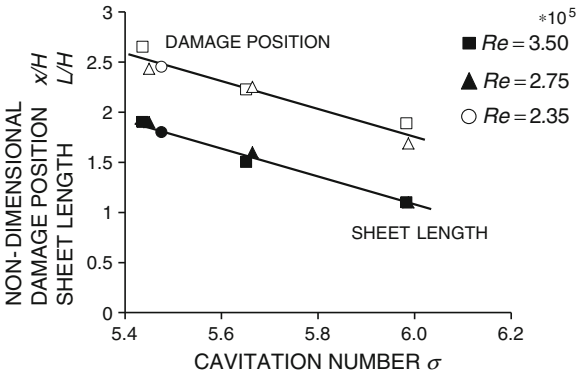

Fig. 9.18 Dimensionless damage position and non-dimensional sheet cavity length for $R^+ = 2.5$

9.5 Conclusions

- For a convergent divergent nozzle, a critical Reynolds number is determined. For Reynolds numbers below that critical value sheet cavitation is observed. For Reynolds numbers above that critical value cloud cavitation is observed.
- The nozzle geometry is such that the minimal radius of curvature can easily be changed. Up to now the radius of curvature was set to 2.5 times the channel height. A small radius of curvature and thus a more divergent nozzle part leads to a more stochastic cavitation.
- By the aid of optical measurements the largest scales of the cavitation phenomena were determined.
- An upper limit for the Strouhal number was observed. That upper limit is dependent on the Reynolds number.
- The circulation of clouds was determined.
- Within the cloud regime there is no influence on the Reynolds number, which justifies model tests of pumps and turbines.
- A dimensionless damage function was defined and the plastic deformation of the material surface was determined as a function of cavitation number.

Acknowledgments The presented results were obtained within the research project No. 16054 N/1, funded by budget resources of the Bundesministerium für Wirtschaft und Technologie (BMWi) approved by the Arbeitsgemeinschaft industrieller Forschungs-vereinigungen "Otto von Guericke" e.V. (AiF).

References

1. Keil T, Pelz PF (2012) On the transition from sheet to cloud cavitation. In: Proceedings of the 8th international symposium on cavitation, CAV2012, Singapore, 13–16 August 2012
2. Buttenbender J, Pelz PF (2012) On the bubble dynamics in cavitation clouds under circulation and strain. In: Proceedings of the 8th international symposium on cavitation, CAV2012, Singapore, 13–16 August 2012

3. Ida M (2004) Investigation of transition frequencies of two acoustically coupled bubbles using a direct numerical simulation technique. J Phys Soc Jpn 73(11):3026–3033
4. Ida M (2009) Multibubble cavitation inception. J Phys Soc Jpn 21(11):113302
5. Konno A, Kato H, Yamaguchi H, Maeda M (2002) On the collapsing behavior of cavitation bubble clusters. JSME Int J Ser B 45(3):631–637
6. Wang YC (1996) Shock waves in bubbly cavitating flows (Part I) Shock waves in cloud cavitation (Part II) Bubbly cavitating flows through a converging-diverging nozzle. PhD thesis, California Institute of Technology, Pasadena
7. Kawanami Y, Kato H, Yamaguchi H, Maeda M, Nakasumi S (2002) Inner structure of cloud cavity on a foil section. JSME Int J Ser B 45(3):638–645
8. Joussellin F, Delannoy Y, Sauvage-Boutar E, Goirand B (1991) Experimental investigations on unsteady attached cavities. ASME Fluids Eng Div 116:61–66
9. Kawanami Y, Kato H, Yamaguchi H, Tagaya Y, Tanimura M (1997) Mechanism and control of cloud cavitation. J Fluids Eng 119:788–794
10. Arndt REA, Hambleton WT, Kawakami E (2009) Creation and maintenance of cavities under horizontal surfaces in steady and gust flows. J Fluids Eng 31:111301-1
11. Lohrberg H (2001) Messung und aktive Kontrolle der erosiven Aggressivität der Kavitation in Turbomaschinen. Fortschritts-Bericht VDI Reihe 8 Nr. 942 ISBN 3-18-394208-5